HHS Public Access

Author manuscript

Magn Reson Med. Author manuscript; available in PMC 2023 February 01.

Published in final edited form as:

Magn Reson Med. 2022 February ; 87(2): 614–628. doi:10.1002/mrm.28992.

External Dynamic InTerference Estimation and Removal (EDITER) for low field MRI

Sai Abitha Srinivas[1,2], **Stephen F Cauley**[3,4], **Jason P Stockmann**[3,4], **Charlotte R Sappo**[1,2], **Christopher E Vaughn**[1,2], **Lawrence L Wald**[3,4,5], **William A Grissom**[1,2,6,7], **Clarissa Z Cooley**[3,4,*]

[1]Vanderbilt University Institute of imaging science, Nashville, TN, United States

[2]Department of Biomedical Engineering, Vanderbilt University, Nashville, TN, United States

[3]Harvard Medical School, Boston, MA, United States

[4]Dept. of Radiology, Massachusetts General Hospital, Athinoula A Martinos Center for Biomedical Imaging, Boston, MA, United States

[5]Harvard-MIT Division of Health Sciences and Technology, Cambridge, MA, United States

[6]Department of Electrical Engineering, Vanderbilt University, Nashville, TN, United States

[7]Department of Radiology, Vanderbilt University, Nashville, TN, United States

Abstract

Purpose: Point-of-care MRI requires operation outside of Faraday shielded rooms normally used to block image-degrading electromagnetic Interference (EMI). To address this, we introduce the EDITER method, an external sensor-based method to retrospectively remove image artifacts from time-varying external interference sources.

Theory and Methods: The method acquires data from multiple EMI detectors (tuned receive coils as well as untuned electrodes placed on the body) simultaneously with the primary MR coil during and between image data acquisition. We calculate impulse response functions dynamically that map the data from the detectors to the time varying artifacts then remove the transformed detected EMI from the MR data. Performance of the EDITER algorithm was assessed in phantom and *in vivo* imaging experiments in an 80mT portable brain MRI in a controlled EMI environment and with an open 47.5mT MRI scanner in an uncontrolled EMI setting.

Results: In the controlled setting, the effectiveness of the EDITER technique was demonstrated for specific types of introduced EMI sources with up to a 97% reduction of structured EMI and up to 76% reduction of broadband EMI in phantom experiments. In the uncontrolled EMI experiments, we demonstrate EMI reductions of up to 99% using an electrode and pick-up coil *in-vivo*. We demonstrate up to a 9-fold improvement in image SNR with the method.

[*]Corresponding author: Clarissa Zimmermann Cooley, Massachusetts General Hospital, Radiology, room 2301, 149 13th Street, Charlestown MA 02129, czcooley@mgh.harvard.edu, Phone: 617-724-1839.

Code availability. The MATLAB code for the algorithm is available at https://github.com/abithasrinivas/EDITER_LowfieldMRI.

Conclusion: The EDITER technique is a flexible and robust method to improve image quality in portable MRI systems with minimal passive shielding and could reduce the reliance of MRI on shielded rooms and allow for truly portable MRI.

Keywords

Low field MRI; Portable MRI; Accessible MRI; Active RF Shielding

Introduction

There is growing interest in low-field, low-cost, and portable MRI scanners for democratizing MRI and extending its use to unconventional locations [1-3]. Specialized brain scanners are a particularly attractive target for this role since the soft tissue contrast of MRI outshines other imaging modalities but can be underutilized due to cost or lack of access [4]. Simplified low-field portable brain scanners could be used as point-of-care (POC) [5 - 18] instruments in hospital EDs and ICUs or as easy-to-site scanners in underserved and unconventional locations (hospitals in the developing world, rural clinics, urgent care clinics, sports arenas, etc.).

However, the traditional surrounding RF-shielded room (“Faraday shield”), which shields the MR scanner from external sources of Electro Magnetic Interference (EMI), precludes portability and flexible POC use. Nuisance electromagnetic signals are generated from a wide variety of external sources (including nearby electronic equipment) and radiation at frequencies close to the Larmor frequency can contaminate the MR signal through electromagnetic induction in the primary MR imaging coils. If unmitigated, the interference can significantly degrade the image quality and reduce diagnostic utility. To enable truly portable MRI devices, alternative approaches to EMI suppression are needed.

One approach is to apply local passive conductive shielding in and around the portable scanner (as opposed to the room). Of course, for dedicated head scanners, these RF shields must have an opening to accommodate the subject’s body but may be built around the outside of the magnet [8,19] or directly exterior to the RF coil [5]. For low-field systems, the shields’ opening is small compared to the Larmor frequency wavelength, and therefore effectively attenuates interference for imaging phantoms contained within the shield. However, when imaging a human subject, EMI is conducted by the body parts external to the magnet and shield and is picked up by the RF coil. This requires that passive shielding encompass the entire body of the patient, for example, using conductive mesh cloth draped over the patient [8]. For maximum effectiveness, the conductive cloth must be completely sealed around the body, which can be uncomfortable and limit access to the patient.

Active and post processing cancellation approaches to EMI mitigation that are more flexible and are less intrusive to the subject have been developed for Magnetotellurics [20-22], transient electromagnetics [23], SQUID MRI [24], surface NMR instrumentation [25-32], ECG [33], EEG [34] and MRI [35-43]. Large “figure 8”-shaped surface coils have also been used to cancel EMI actively [26, 31] for surface NMR groundwater surveys, but this method is not easily translated to in vivo brain imaging. Methods that mitigate EMI effects such as

spiking in an image have been proposed using machine learning and other such advanced signal processing algorithms [35,36], but are model based and generally require training datasets. Common EMI suppression methods for surface NMR include the use of an external or “remote” reference loop wherein a global transfer function is formed from “noise” data (calibration data) both in frequency [30] and time domain [25]. This has been extended to an arbitrary number of external reference loops for more robust performance [32]. Another popular method for noise suppression uses an adaptive filter approach in time domain [37]. We note that EMI mitigation is also needed for other biomedical measurements, such as ECG and EEG, where adaptive filter algorithms have been demonstrated with electrode data [33,34].

In the MR field, an early method by Letcher [38] reduced EMI artifacts with Weiner filter deconvolution. The filter transfer function was formed from the power spectrum of the MR data and calibration data which were sampled by the primary MR receiver during dummy cycles in the acquisition. Similar methods using external detectors have been proposed in the field of MR [39-40] and implemented in a commercial portable MRI system alongside other MR systems [41]. In these methods, calibration data is sampled to form complex global transfer functions similar to existing work in surface NMR, correlating the external EMI coil data to the primary MRI coil data. The reliance on calibration data from pre-scan data alone could hinder the ability to mitigate time-varying EMI sources and could increase scan time if the pre-scans need regular updates.

We propose an approach to dynamic EMI correction using data that is acquired simultaneously during the scan from EMI detectors external to the imaging volume and the primary MR coil. The EMI detectors include external RF coils as well as electrodes attached to the subject. We term our method: External Dynamic InTerference Estimation and Removal (EDITER). Unlike other detector-based EMI suppression methods [39-43], the EDITER method has the advantage of not requiring calibration data or modifications to the imaging sequence, and leverages the data acquired throughout the acquisition to form a dynamic correction model that is robust to time-varying EMI sources. Our dynamic model comprises a kernel that relates the external detectors’ signals to the artifact’s appearance in the signal of a primary imaging coil. Estimated EMI contamination is removed from the primary MR data in postprocessing. Previously, we demonstrated the use of dynamic calibration data collected at the end of each acquisition TR period (acquired during deadtime) to calculate a new transfer function for each line of k-space [44]. Here, we show that this calibration data is not needed and that the model can be fit directly using data acquired during NMR signal reception. Since the signal is simultaneously acquired by both the EMI detectors and the primary MR coil and there are no additional acquisition periods beyond what is needed for imaging, the method can be added to any sequence with no modifications. Using simultaneously acquired data provides the advantage of constraining the model to a compactly supported time-domain kernel which cannot be done using calibration data.

Compared to previous work, instead of forming distinct models for each acquisition line or forming a global model using all acquisition lines (or calibration data), we form multiple models by grouping detector acquisition lines with correlated EMI properties, similar to

TGRAPPA [45,46]. This is more robust to noise compared to using single acquisition lines, while still providing a dynamic solution for EMI changing during the scan [47]. Additionally, the use of multiple acquisition lines provides larger convolution windows to correlate the EMI data which yields more accurate impulse response functions and better EMI removal.

The EDITER method was validated in two low-field MRI systems at different centers using pick-up coils and electrodes as EMI detectors. Phantom and *in-vivo* imaging experiments were performed with an 80mT portable head scanner [5] in a shielded room with controlled EMI sources introduced. Similar experiments were performed in an unshielded open-design head scanner at 47.5mT with uncontrolled EMI sources. We applied the proposed algorithm and show improved image quality in scenarios where EMI is robust and time-varying, thus potentially allowing the operation of portable scanners in EMI-unfriendly environments without a traditional Faraday shielded room.

Theory

EDITER is based on a generalized model that can dynamically adjust to time-varying external noise sources. The model allows for simultaneously acquired data from multiple EMI detectors to be regressed from the primary MR coil data. Here, a linear relationship is assumed between the k-space signal measured by the primary receive coil $s(k_x, k_y)$, the unwanted EMI on the imaging coil $e'(k_x, k_y)$, and the desired EMI-free k-space data $s'(k_x, k_y)$:

$$s(k_x, k_y) = e'(k_x, k_y) + s'(k_x, k_y) \quad \#(\text{eq.1})$$

To allow for accurate estimation and removal of the EMI, we assume that data is available from N_c external detectors $e_i(k_x, k_y)$, $i = 1, \ldots, N_c$. A linear convolution model along the readout (k_x) and phase encoding (k_y) directions relates the EMI observed by the primary imaging coil to that observed by the external detectors:

$$e'(k_x, k_y) = \sum_{i=1}^{N_c} e_i(k_x, k_y) * h_i(k_x, k_y) \quad \#(\text{eq.2})$$

Each impulse response function is assumed to have limited spectral support, i.e., $h_i(k_x, k_y) = 0, |k_x| > \Delta k_x \text{ or } |k_y| > \Delta k_y$. In the most restrictive case, $\Delta k_x = 1$, $\Delta k_y = 1$, (eq. 2) represents a scalar combination of the detector coils:

$$e'(k_x, k_y) = \sum_{i=1}^{N_c} e_i(k_x, k_y) \cdot h_i \quad \#(\text{eq.3})$$

The linear convolutional form of Eq. 2 can be incorporated into Eq. 1 and written in matrix form as: $\vec{s} = \vec{e'} + \vec{s'} = E\vec{h} + \vec{s'}$. The impulse response vector $\vec{h} \in \mathbb{C}^{N_c \Delta k_x \Delta k_y \times 1}$ is a concatenation of the spectral components for the impulse response functions, and the EMI convolution matrix $E \in \mathbb{C}^{N_F \times N_c \Delta k_x \Delta k_y}$ is a block-Toeplitz matrix mapping the EMI

detector coil data to N_F data points in the primary receive coil. An illustration of fitting impulse response functions is shown in Figure 1A. In the case of temporally static EMI, a single set of impulse response functions would be valid across the full extent of k-space and all available data could be used during the fit, i.e. $N_F = N_{k_x} \cdot N_{k_y}$. While k_x and k_y coordinates are used in the present mathematical treatment for familiarity and convenience to index data points within the readouts (k_x) and between readouts (k_y), we note that the method does not depend in any way on the specific k-space sampling trajectory used.

The least squares solution $\vec{h} = E^{\dagger}\vec{s}$ is used to fit the model and the EMI can be removed from the primary coil data as: $\vec{s}' \approx \vec{s} - E\vec{h}$. It is important to note that this method assumes low correlation between the spectral content of the image and noise sources. In the unlikely event that such correlation does exist, this would merely lead to smoothly varying sensitivity loss across the image due to the limited support assumed for each $h_l(k_x, k_y)$ and this amplitude modulation across the image would not normally hinder diagnosis.

We generalize the method to scenarios where EMI sources are time-varying by assuming that each impulse response function applies only to a limited temporal window (e.g. one or more successively acquired phase encode lines) and fit different impulse response functions for each window. As the number of observations in each temporal window becomes small, the estimation robustness will be degraded. To minimize this effect, we dynamically bin the data into larger temporal windows that have consistent EMI patterns. This is accomplished by first constructing a matrix H that contains the $\vec{h}$ vectors generated for the different temporal windows N_w. The Δk_y used to construct the H matrix is restricted to be less than or equal to N_w. Here, we use N_w=1 therefore, Δk_y=1. We then construct a matrix C by autocorrelating the normalized matrix H. Consistent EMI sources will lead to similar impulse response functions which in turn will have high correlation. The binning locations can be determined with standard clustering approaches [48] such as thresholding the correlation matrix C to form $C_{\text{threshold}}$ as shown in Figure 1B. A final pass of the method is then performed to estimate the impulse response functions and remove EMI from each dynamically determined temporal window, and larger values of Δk_y can be used. Pseudocode for the generalized algorithm is provided below:

1. Distribute phase-encoded lines into N_W short temporal windows of size: $W = N_{PE}/N_W$.
2. **For each temporal window $1 \le k \le N_W$:**
   a. Construct convolution matrix: $E_{(k)} \in \mathbb{C}^{(N k_x W) \times N_c \Delta k_x \Delta k_y}$ (Figure 1A).
   b. Arrange primary coil signal into vector: $\vec{s}_{(k)} \in \mathbb{C}^{(N_{RO} W) \times 1}$.
   c. Compute impulse response functions: $\vec{h}_{(k)} = E^{\dagger}_{(k)} \vec{s}_{(k)}$.
3. Calculate impulse response correlation matrix: $C_{i,j} = \langle \vec{h}_{(i)}, \vec{h}_{(j)} \rangle, 1 \le i, j \le N_W$.

4. Cluster temporal windows into N_G groups, e.g. using k-means clustering [48], see Fig. 1B.

5. **For each temporal cluster $1 \leq g \leq N_G$:**

   a. Formulate convolution matrix $E_{(g)}$.

   b. Arrange primary receive signal into the vector: $\vec{\mathbf{s}}_{(g)}$.

   c. Compute impulse response functions: $\vec{\boldsymbol{h}}_{(g)} = \boldsymbol{E}^{\dagger}_{(g)} \vec{\boldsymbol{s}}_{(g)}$.

   d. Remove EMI from primary coil signal: $\vec{\boldsymbol{s}}'_{(g)} = \vec{\boldsymbol{s}}_{(g)} - \boldsymbol{E}_{(g)} \vec{\mathbf{h}}_{(g)}$.

Methods

Experiments in controlled EMI settings in an 80mT portable low-field brain MRI:

A portable, head-only low-field MRI scanner at MGH [5] was used to demonstrate EDITER in phantoms and *in vivo*. The system is based on a compact 122 kg, 80mT permanent magnet Halbach cylinder that requires no power or cooling. The magnet produces a built-in field gradient for readout encoding which obviates a readout gradient system and reduces the system's power and cooling needs. The built-in readout gradient necessitates the use of spin-echo sequences and frequency-swept RF pulses to cover the full Larmor frequency bandwidth [49,50]. Recently published *in vivo* imaging results with this scanner were acquired in a stationary RF-shielded room to attenuate EMI [5].

To validate EDITER, we acquired phantom data in the shielded room with introduced EMI sources to fully control the EMI contamination. This gave us the ability to acquire "ground truth" EMI-free images simply by turning off the sources and also to generate time-varying sources. Four imaging experiments were performed with the following sources introduced: 1) A single coherent frequency source generated with a wire loop that was positioned at the end of the patient table and connected to a frequency generator (FG) producing a 10 Vp-p sine wave at the Larmor frequency (3.38 MHz) of the magnet. 2) A stepper motor (SM) that produced robust sporadic EMI at multiple frequency bands and was positioned behind the magnet. 3) Three cascaded 1W RF power amplifiers (RFPA) (Mini-circuits ZHL− 3A+, NY, USA) that were connected to untuned loops positioned underneath the scanner, to produce broadband (BB) EMI. 4) Time-varying EMI produced by manually switching SM and BB EMI sources during the scan.

Five identical EMI detectors were built from 10-turn coils wound on 3D printed formers (OD = 8 cm) as shown in figure 2C. These EMI detectors were tuned and matched to the Larmor frequency of the scanner (3.38 MHz) with a bandwidth of 25 KHz to achieve a similar frequency response to the primary RF coil. Two detectors were used with 50 ohm, 37 dB gain pre-amplifiers (MITEQ P/N AU 1583, NY, USA) and three detectors were used with 50 ohm, 24 dB gain preamplifiers (Mini-circuits ZHL-500LN+, NY, USA). The placement of the detectors is illustrated in Figures 2D and 2E. EMI detectors 1 and 2 were placed behind the sides of the scanner. EMI detector 3 was placed underneath the scanner. EMI detectors 4 and 5 were placed by the sides of the scanner. EMI detectors 1, 3, 4 and

5 were oriented along the B1 direction. EMI detector 2 was oriented orthogonal to B1 to acquire EMI in an additional vector direction.

Phantom experiments were performed using an MR Solutions (Guilford, UK) console with 32 Rx channels and 4 Tx channels. Other hardware included 2 AE Techron 7224 gradient amplifiers (Elkhart, IN, USA) and a 2kW peak-power RF power amplifier (Tomco Technologies model BT02000-AlphaS-3MHz, Stepney, Australia). Data was acquired using a single-channel RF transmit/receive coil for primary MR data shown in Figures 2A and 2B [13,51] with a 50 ohm, 37 dB gain pre-amplifier (MITEQ P/N AU 1583, NY, USA) and a 24 dB second-stage amplifier (Mini-circuits ZHL-500LN+, NY, USA). Experiments were performed with a 1 cm-thick 3D printed brain slice phantom.

The 2D multi-echo Rapid Acquisition and Relaxation Enhancement (RARE) volumetric spin echo sequence [5, 52] shown in Figure 3 was used to obtain the data shown in Figure 6. The sequence parameters used were: Resolution = 2.2mm x1.3mm, Matrix size = 512 (Read-out) x 101 (Phase Encode). Since this was a 2D phantom, no partition gradient was used for this acquisition.

To further validate EDITER, *in-vivo* experiments were performed in one healthy subject (S1: male, 24 y/o) after providing consent in accordance with the Massachusetts General Hospital Institutional Review Board (IRB) guidelines in a shielded room with the frequency generator (FG) EMI source as described earlier. This was done using a Tecmag Bluestone (Houston, TX, USA) console with 2 Rx channels and 2 Tx channels. The same amplifier hardware and primary RF transmit/receive coil for primary MR data as that in the phantom experiments were used. Here, we only used one EMI detector coil (position 1). A 3D multi-echo Rapid Acquisition and Relaxation Enhancement (RARE) volumetric spin echo sequence [5, 51] as shown in Figure 3 was used to obtain the data. The sequence parameters used were - Resolution = 2.2mm x1.3mm x 9mm, Matrix size = 256 (Read-out) x 97 (In-plane Phase Encode) x 23 (Partition Phase Encode).

EDITER correction was performed on each EMI source data set. The correction was performed with each detector coil individually and with the combined detector data. To determine the impulse response vectors, $\vec{h}$, we used an EMI convolution window size of Δk_x = 7 and Δk_y = 1. In these controlled experiments, we compare the corrected and uncorrected images and quantify the EMI mitigation performance with 2 different metrics. Metric 1 is an RMSE comparison of the image space residual compared to ground truth. Metric 2 estimates the EMI removal percentage using the standard deviation in a region outside the object in the corrected and uncorrected images (equation 4).

$$EMI\ {}^{removal}_{percentage} = \left| \frac{\sigma_{UN} - \sigma_C}{\sigma_{UN}} \right| \times 100\ \% \qquad \#(\text{eq.4})$$

In equation 4, σ_{UN} and σ_C represent the standard deviation of an EMI region in the uncorrected image and the corrected images respectively. The EMI region was chosen so that no part of the object was included in the calculation.

Experiments in uncontrolled settings in a 47.5 mT open low-field system:

Imaging experiments in an anthropomorphic head phantom [53,54] and three human subject*s* were performed at Vanderbilt University with the 47.5 mT permanent magnet MRI scanner shown in Figure 4 (Sigwa MRI, Boston, MA, USA) [55]. The Sigwa scanner weighing 13380 kg is an open, biplanar permanent magnet imaging system with an 80 cm gap and a 2 m x 1.4 m footprint. The B_0 field has 18.7 ppm homogeneity over the center 40 cm DSV and 5 Gauss line approximately 2.5 m from isocenter. The scanner's high homogeneity enabled the use of hard pulse excitations instead of the frequency-swept pulses used for the portable 80 mT scanner described above. Mounted to the magnet pole pieces are 3-axis planar gradient coils with < 6% linearity in a 40 DSV and < 1.25% linearity in a 20 cm DSV. The scanner is controlled with a Tecmag Redstone console (Houston, TX, USA) with two transmit and three receive channels. The gradients are driven by three AE Techron 2120 amplifiers (Elkhart, IN, USA) and a 500W peak-power RF power amplifier was used (Tomco Technologies model BT00500-AlphaS, Stepney, Australia). Images were acquired using a single channel Tx/Rx RF coil [5,13,51] similar to that used the portable head scanner (Figure 4A) and a 50-ohm, 70 dB gain pre-amplifier (MITEQ P/N 1583 10057, NY, USA).

The Sigwa scanner is not sited in an RF shield room. The EMI contamination in these experiments came from uncontrolled environmental sources at Vanderbilt University Medical Center. The phantom and *in vivo* scans were performed with 2 different passive shielding configurations within the magnet (Figure 4c-d). The "open" configuration included a head-sized copper box open on one side surrounding the primary helmet coil (Figure 4C). The "flexible shielding" configuration included the addition of conductive cloth /Faraday shield bedding (Less EMF, NY, USA) draped over the subject (Figure 4D).

For *in vivo* studies, we propose the use of electrodes as EMI detectors to directly measure the EMI that is coupled through the patient [33, 34]. In these experiments, a single electrode (EverOne ECG Monitoring) was attached to the patient's wrist to measure EMI and serves as 1 of 2 of the EMI detectors. The second EMI detector was a pick-up coil with 10 evenly spaced turns on an acrylic former (OD = 5 cm) (Figure 4B). The coil was tuned and matched to the Larmor frequency of the scanner (2.07 MHz) with a similar bandwidth as the primary MR coil (20 KHz). The pick-up coil was positioned alongside the patient oriented in the primary coil's B1 direction as shown in figure 4C and 4D. Both EMI detectors were connected to 50-ohm, 70 dB gain pre-amplifiers (MITEQ P/N 1647, NY, USA). Using the same pick-up coil detector position and attaching ECG electrode to the phantom, studies were done on an anthropomorphic head phantom to illustrate the body antenna effect.

The 3D RARE sequence in Fig. 3 was used to obtain images in the anthropomorphic head phantom [52,53] and *in vivo* scans in three healthy subjects (S1: male, 24 y/o, S2: female, 27 y/o, S3: male, 30y/o). Human subject imaging as done after providing consent in accordance with Vanderbilt university Institutional Review Board (IRB) guidelines. The sequence parameters were: Resolution = 1mm x 2mm x 9mm, Matrix size =128 (Read-out) x 97 (In-plane Phase Encode) x 23 (Partition Phase Encode).

To process the data, we first collapse the two Phase Encoding dimensions to retain continuity in the time domain and then applied the EDITER algorithm to the dataset. We

used an EMI convolution window size of $\Delta k_x = 7$ and $\Delta k_y = 1$ for correction in all datasets. The percent EMI correction was evaluated using Eq. 4. The ground truth RMSE metric was not calculable, as a ground truth was unavailable in these uncontrolled EMI experiments. Additionally, Table 1 details the standard deviation for corrected and uncorrected data for both the flexible and open shielding configurations for the three subjects.

The choice of convolution window widths Δk_x was analyzed by comparing the EMI correction performance as well as the computation time. The computation was done in MATLAB and consisted of loading and reshaping the data and running the EDITER algorithm for all the partitions in the 3D volume. We used MATLAB version 2020a on a MacBook Pro with a 16 GB ram running a 2 GHz Quad-Core Intel Core i5 processor for the computation.

Results

Controlled EMI experiments in 80mT scanner

The four phantom datasets were acquired with the previously described EMI sources introduced: 1) FG, 2) SM, 3) BB, 4) time-varying SM + BB. Supporting information S1 shows the spectra of each EMI source measured by each coil in the experiment. Figure 5 shows the EMI correction correlation matrix (C) for each EMI source. Figures 5A-C show the C matrices for the stationary EMI experiments (FG, SM, BB) showing no significant variation in the correlation between PE lines. Figure 5D shows the correlation matrix for the time-varying EMI source, where the stepper motor (SM) was manually turned “on” for the first half of the image and the broadband (BB) EMI source was turned “on” for the second half. Therefore, we see three separate groups of correlated PE lines ($N_G = 3$) in Figure 5D (the SM period, τ_{SM}, the BB period, τ_{BB}, and the switching period, τ_{Gap}).

Figure 6 shows the 2D phantom imaging results from the controlled-source experiments, including a ground truth image which was acquired with all EMI sources turned off. The uncorrected EMI contaminated images are shown for the 4 acquisitions with the 4 EMI sources. Difference images and RMSE between the uncorrected and ground truth data are also shown. We note that the EMI stripes in the images follow the magnet’s built-in non-linear gradient iso-contours and thus do not appear linear using the general reconstruction method used here, which is further detailed in [5]. The EMI corrected images are shown for each source using all 5 EMI pickup coils. Supporting Information S2 shows the corrected images using each EMI detector individually to demonstrate the contribution of each detector. Figure 6 includes the residual of the corrected images and RMSE compared to the ground truth. Comparing the RMSE, shows a reduction by the EMI mitigation method of 89.2%, 95.7%, 74.7%, and 93.3% in the 4 acquisitions. Comparing the uncorrected to corrected images directly shows an EMI removal percentage of 96.6%, 97.3%, 76.2%, and 86.8% using equation 4.

Although we applied the dynamic EMI correction algorithm, the stationary EMI source experiments (FG, SM, and BB) used single temporal window ($N_G = 1$) for the correction because of the strong correlation of the impulse response across all PE lines (Figure 5). On the other hand, the time-varying EMI source (EMI 4: SM+BB) was corrected with $N_G =$

3 temporal windows. To illustrate the effect of the dynamic vs. static EMI correction, we also show the SM+BB correction with a static impulse response in Figure 6. The dynamic correction resulted in an RMSE improvement of 93.3% and an EMI removal percentage of 86.8%, compared to 73.7% and 70.4% with the static correction.

In vivo results using the FG EMI source are shown in Supporting Information Figure S3. Both the uncorrected EMI contaminated images and EDITER corrected images are shown along with difference images. The RMSE between the uncorrected image and ground truth averaged across partitions is 18.0. The RMSE between the corrected image and ground truth averaged across partitions is 1.57, showing a 91.3% RMSE reduction. Comparing the uncorrected to corrected images directly shows an EMI removal percentage of 91.3% (Eq. 4).

Uncontrolled EMI experiments in 47.5mT scanner

Imaging experiments were performed in the 47.5mT scanner in both “open” and “flexible shielding” configuration (Figure 4C-D). The scanner room was unshielded and contained several uncontrolled EMI sources; usage of devices such as laptops and mobile phones were not restricted within the room to provide a realistic setting. Figures 7A and 7B show PD-weighted images of an anthropomorphic head phantom in the “open” configuration and “flexible shielding” configuration respectively. Figures 8A and 8B respectively show PD-weighted images of Subject 1 (male, 25 y/o) in the “open” configuration and in the “flexible shielding” configuration. Figures 7 and 8 show the EMI-corrected images using each EMI detector (the pickup coil and electrode) individually and together.

For phantom studies (Fig. 7), comparing the detector performance with the EMI removal percentage metric (eq. 4), the pickup coil removed 43.6% and 47.7% of EMI, the electrode removed 6.84% and 20.1% of EMI, and their combination removed 44.7% and 66.1% of EMI in the “open” and “flexible shielding” configuration respectively. The SNRs for the corrected images using both detectors in the “open” and “flexible” shielding configurations were 6.229 and 49.90, respectively. The SNRs for the uncorrected images in the “open” and “flexible” shielding configurations were 3.236 and 9.111, respectively.

For *in-vivo* images (Fig. 8), comparing the detector performance with the EMI removal percentage metric (eq. 4), the pickup coil removed 37.2% and 23.2% of the EMI, the electrode removed 89.9% and 64.6% of EMI, and the combination removed 90.2% and 99.9% of EMI in the “open” and “flexible shielding” configuration, respectively. The SNRs for the corrected images using both detectors in the “open” and “flexible” shielding configurations were 89.19 and 225.2, respectively. The SNRs for the uncorrected images in the “open” and “flexible” shielding configurations were 8.982 and 43.97, respectively. Results in two other subjects including SNR values are shown in Supporting Information Figures S4 and S5 to demonstrate repeatability. Table 1 details the standard deviation for corrected and uncorrected data for both the flexible and open shielding configurations for the three subjects.

In the presented results, we used an EMI convolution window size of $\Delta k_x = 7$, $\Delta k_y = 1$ to compute the impulse response function of each temporal cluster The choice of convolution

window widths Δk_x, is analyzed in Figure 9. Figure 9A shows the EMI removal percentage (eq. 4) versus Δk_x for the 3 *in vivo* datasets acquired in the 47.5mT scanner. Figure 9B shows the computation time averaged across all subjects versus Δk_x. Results show that increasing the convolution window width improves the EMI correction performance but increases computation time. We see diminishing returns on the EMI correction for $\Delta k_x > 4$ and a steep increase in computation time for $\Delta k_x > 8$, suggesting $4 < \Delta k_x < 8$ as a good choice for the algorithm. In this analysis and in the imaging results, we set $\Delta k_y = 1$. While a 2D convolution window is possible, we did not observe any advantage in performance with $\Delta k_y > 1$.

Discussion

The proposed dynamic EMI mitigation method (EDITER) is efficient and straightforward to integrate with POC imaging systems. It was successfully applied to remove EMI in phantom imaging and *in vivo* imaging in two different low-field MRI systems. In a comparison to "ground truth" images obtained in the 80mT, EDITER achieved a total image space RMSE reduction of up to 95.7% and up to a 97.3% EMI removal percentage in the standard deviation of the image background (eq. 4).

For uncontrolled EMI settings, we demonstrated up to a 99.9% EMI removal percentage in *in vivo* imaging results using Eq.4. The three *in vivo* imaging datasets were acquired over the course of 57 days and were corrupted by different environmental EMI levels and patterns. Table 1 shows the lowest EMI was achieved with the flexible shielding and EDITER correction. On average, compared to the open shielded uncorrected data, the EDITER correction alone decreased EMI by 71.8%, the flexible shielding alone decreased EMI by 67.3%, and combined they decreased EMI by 89.9%. The flexible shielding alone was much more effective in some cases than others. For example, Subject 2 uncorrected EMI had a relative standard deviation (RSD) of 44.9% in the open configuration and an RSD of 10.7% in the flexible shielding configuration. On the other hand, even with the flexible shielding, Subject 3's uncorrected EMI level had an RSD of 33.2%, but this reduced by 78.8% to RSD = 7.04% with EDITER method. This disparity could be related to the characteristics of the EMI or from variability in setting up of the flexible shielding mesh.

Our dynamic method could be useful in mitigating spatiotemporally varying EMI in new portable MRI settings such as in ambulances or at the bedside. This is accomplished by grouping phase encode lines into correlated temporal windows and creating separate impulse responses ($\vec{h}$) for each group. Instead of PE grouping, we could estimate separate impulses responses for each PE line. However, the use of several PE lines corresponds to a longer EMI convolution matrix (E) and a better conditioned impulse response estimation. In fact, for static/stationary EMI, the correction is done by grouping all PE lines together for calculation of a single $\vec{h}$ for the dataset. The effectiveness of using the dynamic PE grouping as opposed to the static method is illustrated in Figure 6 for the time-varying EMI example. We see an improvement of 75% when using the dynamic PE grouping. We also found that increasing the convolution window size to $\Delta k_x > 1$ aids the correction up to a certain point but can require longer processing time and thus there is a tradeoff between

amount of correction and time utilized (figure 9). Although the scanners we used for in vivo experiments were stationery, the N_G grouping we saw for some of the results was greater than 1. We might expect higher N_G values for truly portable MR scanners.

Detector positioning is quite important to make the EMI mitigation effective. Supporting Information figure S1 shows the EMI spectra as seen by the primary MR coil and the different EMI detectors for the controlled EMI sources in the shielded room. Observing the EMI detector placement in Figure 2D and 2E, EMI detectors 4 and 5 were closest to the single-band (frequency generator) EMI source. Not surprisingly, in Figure S1 A we see that those detectors (4 and 5) picked up the highest amplitude signals from that source. Similarly, the stepper motor EMI source was closest to EMI detectors 1 and 2 and the broadband source is closest to detector 3 which fit with the spectra seen in Figure S1 B and S1 C, respectively. Finally, when the time-varying source was a combination of stepper motor and broadband sources, EMI detectors 1, 2 and 3 were closest to these sources as illustrated by the spectra seen in Figure S1 D. In Supporting Information Figure 2, we see the correction resulting from each detector coil individually. The figure shows that different detectors perform better for different sources based on their position with respect to the source. In a real-world scenario, since the EMI source locations and orientations is unknown, this suggests that it will be beneficial to use multiple detectors distributed around the scanner.

In the 47.5mT scanner experiments, two different types of external EMI detectors were used, i.e., a tuned and matched pickup coil and an untuned electrode. In the phantom studies, the EMI reduction from the pickup coil data was higher than from the electrode data. For the *in vivo* studies, we found the electrode detector was more effective than the pickup coil detector, but the combined use of both yielded the best results. This suggests that the electrode is more effective for removing the EMI piped in by the body-antenna effect, and that the tuned pickup coil is effective for removing EMI directly picked up by the primary coil. We predicted that the pickup coil would detect similar EMI patterns to the primary MR coil because of the similar frequency response and detection mechanism. However, we found that sampled EMI patterns relied heavily on the detector orientation and position with respect to the EMI source. This points to the need for a greater number of pick-up coils in several orientations. Additionally, the geometry and size of the primary RF coil was different than that of the detector coils which may also cause disparities in the received signals. The electrode on the other hand is non-resonant and picks up EMI-induced potentials on the human body which will presumably be “piped in” into the imaging coil regardless of the detectors’ positioning with respect to the EMI sources. Because the electrode is untuned, it likely receives EMI that is also outside the MR acquisition bandwidth and the amplifier system could become saturated by this out-of-band signal. Thus, the use of a band pass filter may improve results.

We use a total of 6 Rx channels for the controlled EMI data and 3 Rx channels for the uncontrolled EMI data which includes 1 Rx channel for the primary MR coil. Using additional Rx channels adds cost and is at odds with the goal of trying to keep spectrometer costs low. Less expensive options for this include using phase shifters or time domain multiplexing [56] for the received signal in order to receive data from one signal Rx channel. Additionally, a low-cost external receiver [57] with a low sampling rate can be used wherein

the signal from the Rx channels can be mixed down and read into the spectrometer using a single Rx channel.

Conclusion

This work described and validated EDITER, an efficient retrospective method for EMI mitigation for time-varying EMI for point-of-care MRI. No additional scan time or pre-scan EMI calibration are required since all the EMI data is acquired simultaneously with the primary MR coil by the EMI detectors. The use of EDITER was evaluated on two separate low field scanners to demonstrate its generality and portability. We made use of a shielded room and controllable EMI sources to provide a direct comparison between a "ground truth" image versus our EMI mitigation images with our method for both *in-vivo* and phantom studies. We also demonstrated EDITER with phantom and *in vivo* imaging in 3 subjects in the presence of uncontrolled EMI with different passive shielding configurations. We showed that different types of EMI detectors can be used such as RF pick up coils and electrodes and that the latter can directly pick-up EMI from the subject specifically for in-vivo scans which can account for EMI originating from various directions that may not be effectively picked up by RF coils which are oriented to specific directions. We showed the EDITER method reduced EMI image artifacts significantly, improving SNR up to a factor of 9. The addition of flexible passive shielding with a draped conductive reduced EMI further in our results. The addition of the EDITER method to compact MRI systems could help bridge the gap to truly portable MRI systems that can be easily sited and re-sited anywhere without a shielded room by mitigating one of the most critical problems in POC low field imaging where SNR is of the essence and passive shield options are limited.

Supplementary Material

Refer to Web version on PubMed Central for supplementary material.

Acknowledgements

We thank Monika Sliwiak for help with 3D design and mechanical construction of RF coil assemblies. We acknowledge Patrick C McDaniel for his role in the developing the 80mT portable scanner. The authors would like to acknowledge Matthieu Sarracanie, Najat Salameh, Cristen LaPierre, Matthew S Rosen and Neha Koonjoo for their past work on the spiral head volume coil and assistance with our implementation of the coil. The research reported in this publication was supported by the National Institutes of Health grants R01EB018976, 5T32EB1680 and R01 EB030414.

References

[1]. Wald LL, McDaniel PC, Witzel T, Stockmann JP and Cooley CZ. Low-cost and portable MRI. J. Magn. Reson. Imaging 2020. doi: 10.1002/jmri.26942.

[2]. Marques JP, Simonis FFJ, and Webb AG. Low-field MRI: An MR physics perspective. J. Magn. Reson. Imaging 2019. doi: 10.1002/jmri.26637.

[3]. Sarracanie M and Salameh N. Low-field MRI: How low can we go? A fresh view on an old debate. Front Phys. 2020. doi: 10.3389/fphy.2020.00172

[4]. Geethanath S and Vaughan JT. Accessible magnetic resonance imaging: A review. J Magn Reson Imaging. 2019. doi: 10.1002/jmri.26638.

[5]. Cooley CZ, McDaniel PC, Stockmann JP. et al. A portable scanner for magnetic resonance imaging of the brain," Nat Biomed Eng. 2020. doi: 10.1038/s41551-020-00641-5.

[6]. McDaniel PC, Cooley CZ, Stockmann JP, Wald LL. The MR Cap: a single-sided MRI system designed for potential point-of-care limited field-of-view brain imaging. Magn Reson Med. 2019. doi: 10.1006/jmre.2000.2263

[7]. Mateen FJ, Cooley CZ, Stockmann JP, Rice DR, Vogel AC and Wald LL. Low-field portable brain MRI in CNS demyelinating disease. Mult Scler Relat Disord. 2021. doi: 10.1016/j.msard.2021.102903. Epub ahead of print. PMID: 33780808.

[8]. O'Reilly T, Teeuwisse WM, de Gans D, Koolstra K and Webb AG. In vivo 3D brain and extremity MRI at 50 mT using a permanent magnet Halbach array. Magn Reson Med. 2021. doi: 10.1002/mrm.28396.

[9]. Ren ZH, Mu WC and Huang SY Design and Optimization of a Ring-Pair Permanent Magnet Array for Head Imaging in a Low-Field Portable MRI System. IEEE Trans. Magn 2019. doi: 10.1109/TMAG.2018.2876679

[10]. Sarty GE and Vidarsson L Magnetic resonance imaging with RF encoding on curved natural slices. Magn. Reson. Imaging 2018. doi: 10.1016/j.mri.2017.10.007

[11]. Lother S, Schiff SJ, Neuberger T, Jakob PM and Fidler F. Design of a mobile, homogeneous, and efficient electromagnet with a large field of view for neonatal low-field MRI. Magn Reson Mater Phys. 2016. doi: 10.1007/s10334-016-0525-8

[12]. Sheth KN, Mazurek MH, Yuen MM, et al. Assessment of Brain Injury Using Portable, Low-Field Magnetic Resonance Imaging at the Bedside of Critically Ill Patients. JAMA Neurol. 2021. doi:10.1001/jamaneurol.2020.3263

[13]. Sarracanie M, LaPierre CD, Salameh N, Waddington DEJ, Witzel T and Rosen MS. Low-cost high-performance MRI. Sci Rep. 2015. doi: 10.1038/srep15177

[14]. Hyperfine - Portable MR Imaging: Bringing MRI to the Patient. https://hyperfine.io/?gclid=Cj0KCQiAx9mABhD0ARIsAEfpavS44Ax2KT5LfC36K95GbfZRUMXzf-jyhkn0uwexFSyjqf933fxu5qAaAszcEALw_wcB. Accessed Jan. 31, 2021.

[15]. Promaxo. Modular MRI System for Use in a Doctor's Office. https://promaxo.com/.Accessed Apr. 27 2021.

[16]. Panther A, Thevathasen, Connell IRO et al. A dedicated head-only MRI scanner for point-of-care Imaging. In proceedings of the 26th Annual Meeting of ISMRM. 2018. p.3679.

[17]. EvryTM. Synaptive Medical. https://www.synaptivemedical.com/products/evry/. Accessed Apr. 27 2021.

[18]. Obungoloch J, Harper JR, Consevage S et al. Design of a sustainable prepolarizing magnetic resonance imaging system for infant hydrocephalus. MAGMA. 2018. doi: 10.1007/s10334-018-0683-y

[19]. Esaote. Dedicated MRI. https://www.esaote.com/en-US/dedicated-mri/. Accessed Apr. 27 2021.

[20]. Gamble TD, Goubau WM and Clarke J. Error analysis for remote reference magnetotellurics. Geophysics. 1979. P959–P968.

[21]. Gamble TD, Goubau WM and Clarke J. Magnetotellurics with a remote magnetic reference. Geophysics. 1979. 44(1), P53–P68.

[22]. Goubau WM., Maxton PM, Koch RH and Clarke J. Noise correlation lengths in remote reference magnetotellurics. Geophysics. 1984. 49(4), P433–P438.

[23]. Spies BR. Local noise prediction filtering for central induction transient electro- magnetic sounding. Geophysics. 1988. 53(8), 1068–1079.

[24]. Espy Michelle A., Magnelind Per E., Matlashov Andrei N., et al. "Progress toward a deployable SQUID-based ultra-low field MRI system for anatomical imaging. IEEE Transactions on Applied Superconductivity. 2014. doi:10.1109/TASC.2014.2365473

[25]. Radic T. Improving the Signal-to-Noise Ratio of Surface NMR Data Due to the Remote Reference Technique. In proceedings of the 12th European Meeting of Environmental and Engineering Geophysics. 2006.

[26]. Walsh DO. Multi-channel surface NMR instrumentation and software for 1D/2D groundwater investigations. Journal of Applied Geophysics. 2008. doi: 0.1016/j.jappgeo.2008.03.006.

[27]. Walsh DO. Multi-channel MRS instrumentation and software for enhanced noise mitigation and 2D/3D imaging. In proceedings of the 3rd Magnetic Resonance Sounding International Workshop. 2006. pp. 73–76

[28]. Grunewald E and Walsh DO. Recent advancements and applications of logging and surface magnetic resonance for groundwater investigations. ASEG Extended Abstracts. 2018.

[29]. Müller-Petke M Non-remote reference noise cancellation-using reference data in the presence of surface-NMR signals. Journal of Applied Geophysics. 2020. doi: 10.1016/j.jappgeo.2020.104040.

[30]. Mueller-Petke M and Yaramanci U. Improving the Signal-to-noise Ratio of Surface- NMR Measurements by Reference Channel Based Noise Cancellation. In Proceedings of Near Surface 16th European Meeting of Environmental and Engineering Geophysics. 2010.

[31]. Trushkin DV, Shushakov O and Legchenko AV. The potential of a noise-reducing antenna for surface NMR groundwater surveys in the earth's magnetic field. Geophysical Prospecting. 1994.

[32]. Neyer F. Surface Nuclear Magnetic Resonance: Processing of Full Time Series, Multichannel Surface NMR Signals, Master's thesis, ETH Zurich, Department of Earth Sciences. 2010.

[33]. Ren A, Du Z, Li J, Hu F, Yang X and Abbas H. Adaptive Interference Cancellation of ECG Signals. Sensors. 2017. doi: 10.3390/s17050942.

[34]. Darroudi A, Parchami J, Razavi MK, and Sarbisheie G. EEG adaptive noise cancellation using information theoretic approach. Biomed Mater Eng. 2017. doi: 10.3233/BME-171680.

[35]. Koonjoo N, Zhu B, Bagnall GC, Bhutto D and Rosen MS. Boosting the signal-to-noise of low-field MRI with deep learning image reconstruction. Sci Rep. 2021. doi: 10.1038/s41598-021-87482-7

[36]. Larsen JJ, Dalgaard E, Auken E. Noise cancelling of MRS signals combining model-based removal of powerline harmonics and multichannel Wiener filtering. Geophysical Journal International. 2014. doi: 10.1093/gji/ggt422

[37]. Dalgaard E, Auken E, & Larsen J. Adaptive noise cancelling of multichannel magnetic resonance sounding signals. Geophysical Journal International. 2012. doi: 10.1111/j.1365-246X.2012.05618.x

[38]. Letcher JH. The use of wiener deconvolution (an optimal filter) in nuclear magnetic resonance imaging. Int J Imaging Syst Technol. 1989. doi: 10.1002/ima.1850010112.

[39]. Rearick T, Charvat G, Rosen MS, and Rothberg J. Noise Suppression Methods and Apparatus. US Patent 9,797,971. March 10, 2016.

[40]. Hushek SG, Saunders J and Schellenberg J. Automatic noise cancellation for unshielded mr systems. International Patent WO2008022441A1. February 28, 2008.

[41]. Harvey PR, Duijvestijn MJ, and Lorenc S. Magnetic resonance imaging with RF noise detection coils. US Patent 10,317,502. June 11, 2019.

[42]. Dyvorne H, Rearick T, Poole M et.al. Freeing MRI from its faraday cage with interference rejection. In proceedings of the 29th Annual Meeting of ISMRM. 2021. P.0749.

[43]. Hrovat M and Dabaghyan M. Noise Cancellation for a Portable MR System In proceedings of the 54th Annual meeting of ENC. Asilomar, CA. 2013.

[44]. Srinivas SA, Cooley CZ, Stockmann JP, McDaniel PC and Wald LL. Retrospective Electromagnetic interference mitigation in a portable low field MRI system. In proceedings of the 28th Annual Meeting of ISMRM. 2020. p.1269.

[45]. Breuer FA, Kellman P, Griswold MA and Jakob PM. Dynamic autocalibrated parallel imaging using temporal GRAPPA (TGRAPPA). Magn. Reson Med. 2005. doi: 10.1002/mrm.20430.

[46]. Griswold MA, Jakob PM, Heidemann RM et al. Generalized autocalibrating partially parallel acquisitions (GRAPPA). Magn Reson Med. 2002. doi: 10.1002/mrm.10171.

[47]. Srinivas SA, Cauley SF, Stockmann JP, Sappo CR, Vaughn CE, Grissom WA, Wald LL and Cooley CZ. In vivo human imaging on a 47.5mT open MRI system with active Electromagnetic Interference (EMI) mitigation using an electrode. In proceedings of the 29th Annual Meeting of ISMRM. 2021. p.4030.

[48]. Hartigan JA, and Wong MA. Algorithm AS 136: A K-Means Clustering Algorithm. Appl Stat. 1979. doi: 10.2307/2346830.

[49]. Stockmann JP, Cooley CZ, Guerin B, Rosen MS and Wald LL. Transmit Array Spatial Encoding (TRASE) using broadband WURST pulses for RF spatial encoding in inhomogeneous B0 fields. J Magn Reson. 2016, doi: 10.1016/j.jmr.2016.04.005.

[50]. Casabianca LB, Mohr D., Mandal S., Song Y and Frydman L. Chirped CPMG for well-logging NMR applications. J Magn Reson. 2014. doi: 10.1016/j.jmr.2014.02.025.

[51]. LaPierre C, Sarracanie M, Waddington DEJ and Rosen MS. A single channel spiral volume coil for in vivo imaging of the whole human brain at 6.5 mT. In proceedings of the Proc. 23rd Annual Meeting of ISMRM, Toronto, CA. 2015. p. 1793.

[52]. Hennig J, Nauerth A, and Friedburg H. RARE imaging: a fast imaging method for clinical MR. Magn Reson Med. 1986. doi: 10.1002/mrm.1910030602.

[53]. Guérin B, Stockmann JP, Baboli M, Torrado-Carvajal A, Stenger AV and Wald LL. Robust time-shifted spoke pulse design in the presence of large B0 variations with simultaneous reduction of through-plane dephasing, B1+ effects, and the specific absorption rate using parallel transmission. Magn Reson Imag. 2015. doi: 10.1002/mrm.25902

[54]. Graedel NN, Polimeni JR, Guerin B, Gagoski B and Wald LL. An anatomically realistic temperature phantom for radiofrequency heating measurements. Magn. Reson. Med. 2015. doi: 10.1002/mrm.25123.

[55]. Coffey AM, Feldman MA, Shchepin RV. et al. High-resolution hyperpolarized in vivo metabolic 13C spectroscopy at low magnetic field (48.7 mT) following murine tail-vein injection. J Magn Reson. 2017. doi: 10.1016/j.jmr.2017.06.009.

[56]. Bankson JA, Griswold MA, Wright SM, and Sodickson DK. SMASH imaging with an eight element multiplexed RF coil array. MAGMA. 2000. doi: 10.1007/BF02601844

[57]. Hasselwander CJ, Cao Z and Grissom WA. gr-MRI: A software package for magnetic resonance imaging using software defined radios. J Magn Reson. 2016. doi: 10.1016/j.jmr.2016.06.023

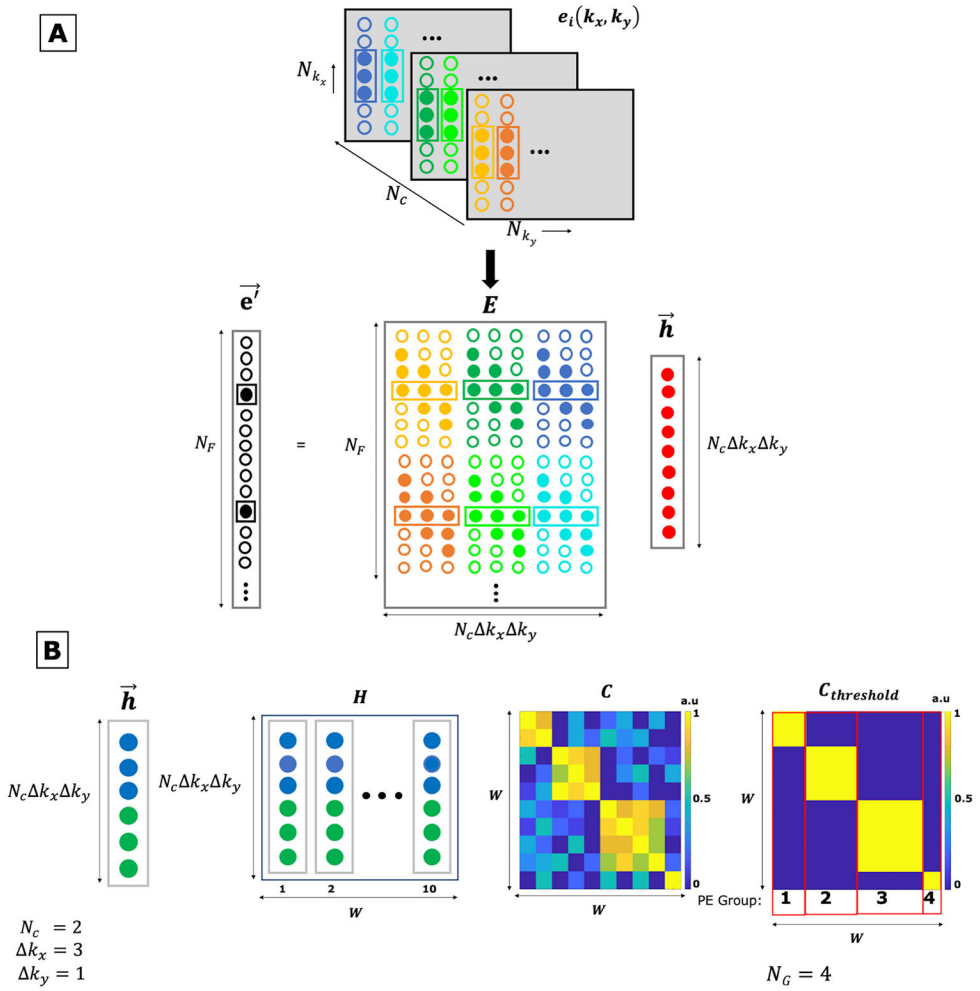

Figure 1: EDITER EMI estimation overview.

A) Fitting Impulse Responses. Top: The k-space data of the external EMI detectors $e(k_x, k_y)$ is acquired simultaneously with the imaging data from all the EMI detectors (N_C). Bottom: The EMI present in the primary image, $\vec{e'}$, is estimated with the impulse response function $\vec{h}$ and the EMI convolution matrix E. E comprises of shifted copies of the phase encode lines with a convolution window size $\Delta k_X = 3$ and $\Delta k_Y = 1$ for all EMI detectors. The impulse response is obtained using the inverse of the EMI convolution matrix E and the primary MR coil data.

B) Dynamic Phase Encode Binning method. Left to right – First, we form an impulse response function h for each temporal group of PE lines individually (W). Here shown for two EMI detectors ($N_c = 2$, blue and green) and a convolution window $\Delta k_X = 3$ and $\Delta k_Y = 1$. The individual impulse response functions are concatenated to form the H matrix with size ($Nc \times \Delta k_X \times \Delta k_Y$) × W (Here, W = 10). We then form a correlation matrix $C = H'H$ wherein H is normalized. This matrix is then clustered using a thresholding value of r = 0.5 to form a binary matrix $C_{threshold}$ that is used to group phase encode lines. Here, we arrive at four groups ($N_G = 4$) with two, three, four and one phase encode lines each.

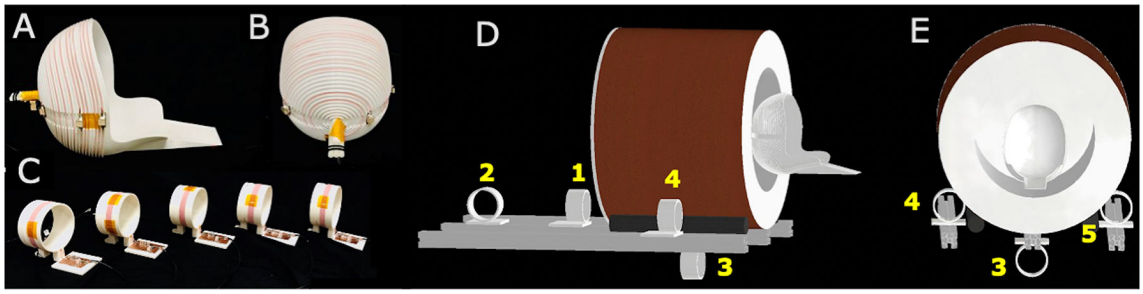

Figure 2: Experimental setup for portable 80mT scanner.

(A-B) The single channel primary MR spiral volume Tx/Rx coil tuned to 3.38MHz for the portable 80 mT scanner with 25 KHz BW. C) Five external EMI detector coils were placed outside the magnet tuned to the Larmor frequency 3.38MHz with a 25KHz BW to mimic the frequency response of the primary MR coil. D-E) Placement of the EMI detector coils around the outside of the portable 80mT head scanner. The yellow numbers indicate the detector channel number.

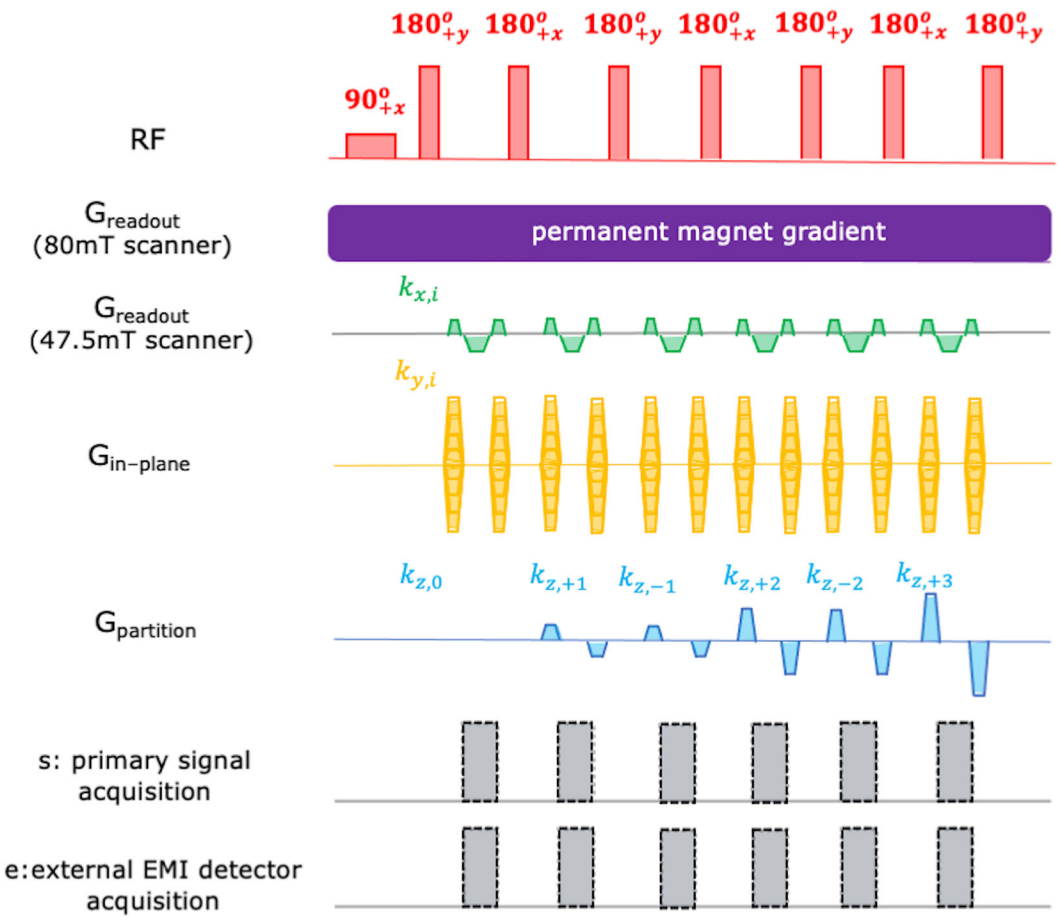

Figure 3: The 3D RARE (Rapid Imaging with Refocused Echoes) pulse sequence used for PD-weighted imaging in both the scanners.

The $G_{readout}$ gradient was the built-in permanent magnet encoding field for the portable 80mT low field head scanner and therefore was continuously applied throughout the acquisition. A conventional pulsed readout gradient as shown in the fourth row was played out in the 47.5mT open low field system. The $G_{in\text{-}phase}$ and $G_{partition}$ phase encoding blips were applied using dedicated gradient coils for both systems. The signal acquisition alternated between the narrow “FID echoes” and wider “spectral echoes” in the portable 80mT scanner. Only “FID echoes” were generated in the 47.5mT low field scanner using hard pulse excitation and refocusing. Data was acquired simultaneously in the primary MR coils and the external EMI coils.

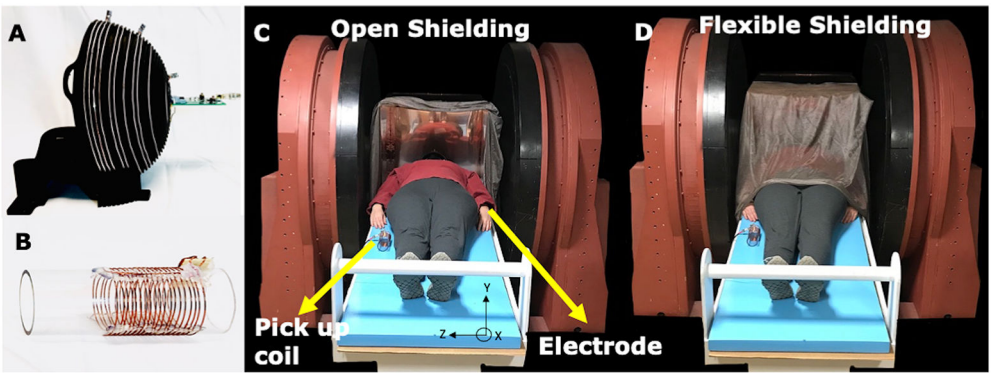

Figure 4: Experimental setup for open 47.5mT scanner.

A) The primary MR coil used for imaging (same spiral design as Fig. 2) tuned to 2.075 MHz with 20 KHz BW. B) EMI detector #1 is a tuned 10 turn RF pick up coil with diameter = 5cm. EMI detector #2 is an ECG electrode (not shown). C-D) The open 47.5mT low field scanner shown with subject and the two EMI detectors, including the electrode attached to subject's wrist. Experiments were performed in 2 shielding configurations. C) The open shielding configuration included a copper box surrounding the head open on one side. D) The flexible shielding configuration included the addition of copper mesh, grounded to the copper box and draped over the subject.

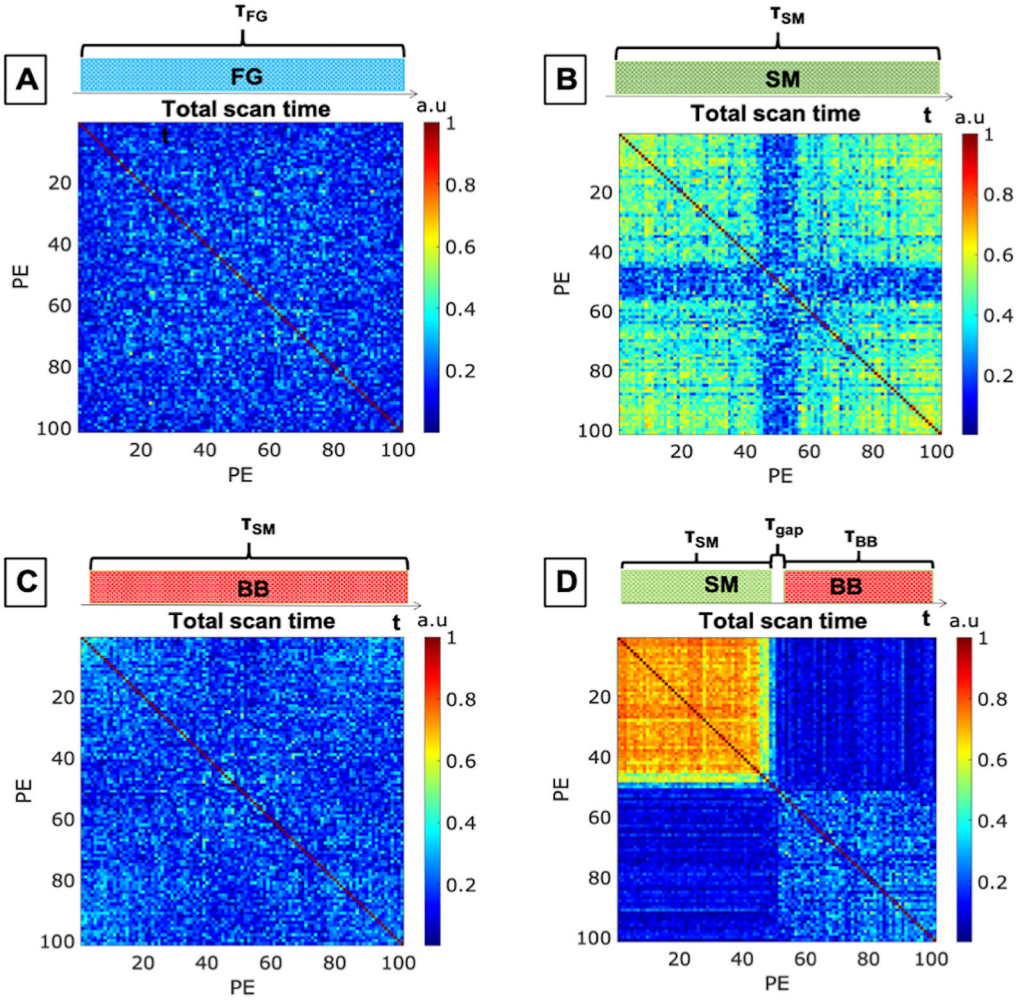

Figure 5: Correlation matrices C for the phantom experiments conducted on the portable 80mT scanner with the following introduced EMI.

A) single band EMI produced by a function generator (FG). B) Narrowband EMI produced by a stepper motor (SM). C) Broadband EMI (BB). D) Dynamic switching between the SM and BB sources (narrowband stepper motor source on during the first half of the scan and broadband EMI source on during the second half).

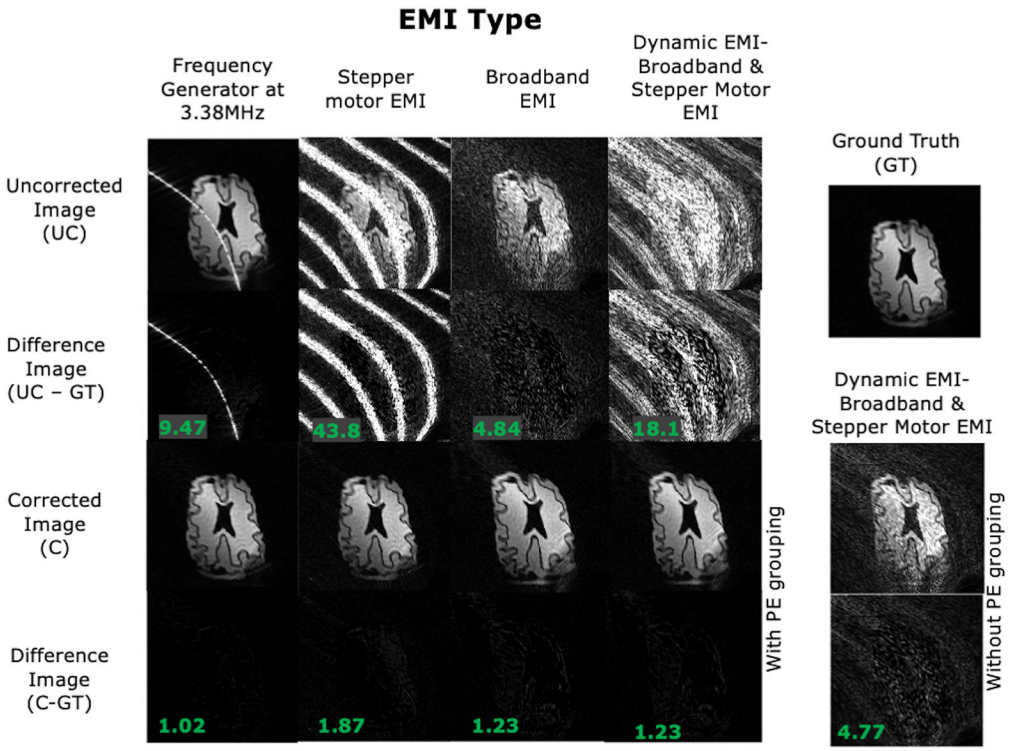

Figure 6: EDITER-corrected 2D images of a brain slice phantom acquired in the portable 80mT scanner.

Results are shown for the 4 introduced EMI sources describe in Fig. 5. Top to bottom: Uncorrected image, Difference images between uncorrected image and ground truth, EDITER-corrected image using all EMI detectors and Difference images between corrected image and ground truth. The RMSE of the difference images is shown in the bottom left. For the dynamic EMI source (SM+BB), we show the EDITER correction with dynamic PE grouping and without grouping - where a single impulse response is calculated for all PE lines.

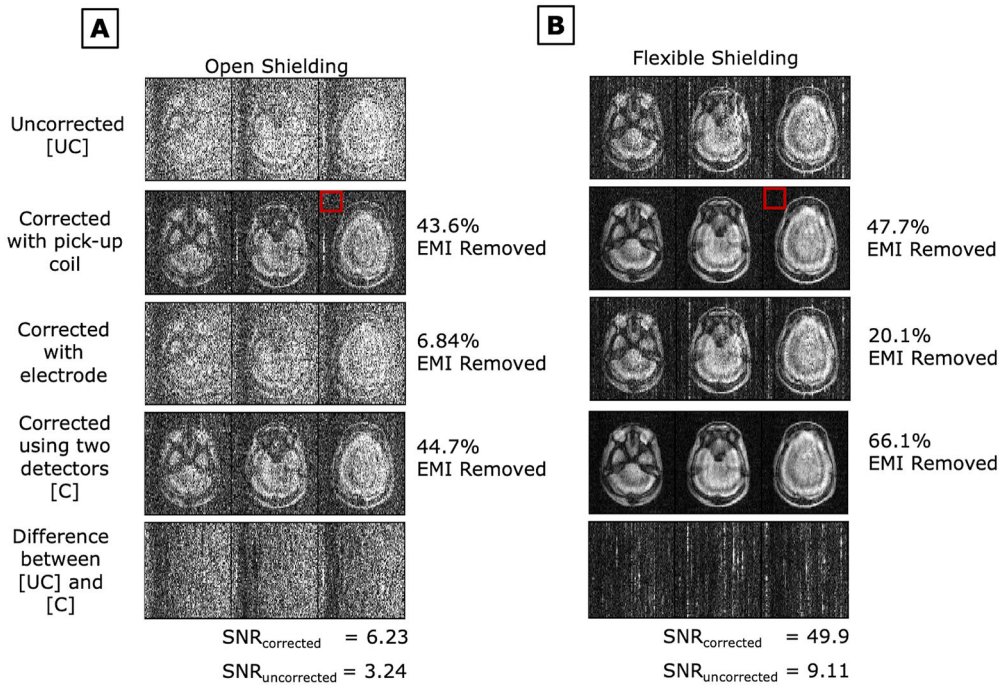

Figure 7:

PD weighted images of an anthropomorphic head phantom in the 47.5mT scanner's A) open shielding configuration setup and B) flexible shielding configuration setup (with draped copper mesh). EDITER correction is shown using each EMI detector individually and together. Percent EMI removed by the EDITER method using Eq.4 is indicated on the right. The red box indicates the region outside the object that was used for this measurement. SNR for both the uncorrected and corrected images are shown.

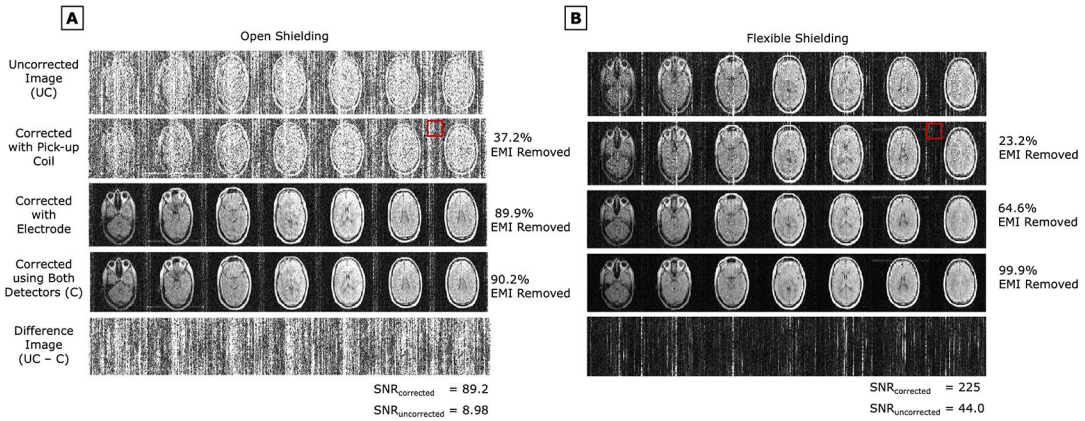

Figure 8:

***in-vivo* PD weighted images of Subject 1** (male, 25 y/o) in the 47.5mT scanner's A) open shielding configuration setup and B) flexible shielding configuration setup (with draped copper mesh). EDITER correction is shown using each EMI detector individually and together. Percent EMI removed by the EDITER method using Eq.4 is indicated on the right. The red box indicates the region outside the object that was used for this measurement. SNR for both the uncorrected and corrected images are shown.

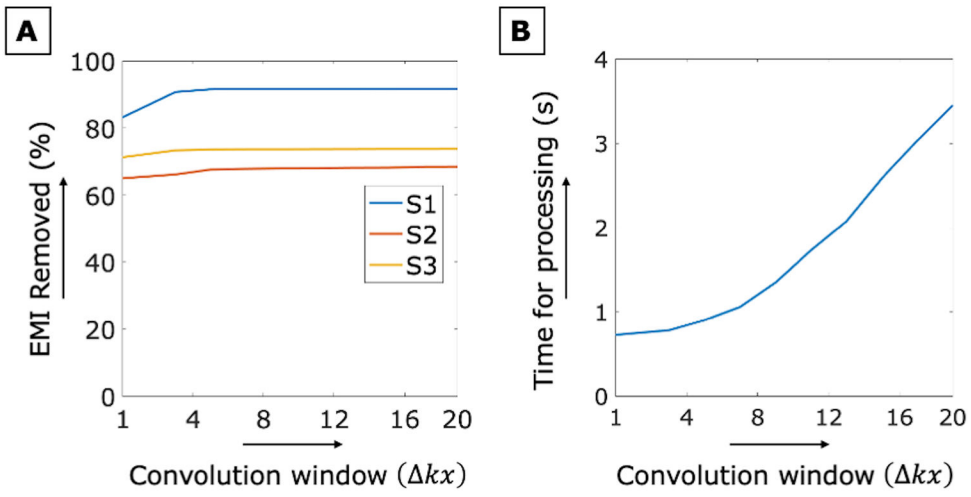

Figure 9:

A) Percent EMI removed using Eq.4 versus the convolution window size Δk_x is shown for the three subjects in the 47.5mT scanner with uncontrolled EMI sources. Results are shown using both EMI detectors in the "open shielding" configuration. B) The average EDITER algorithm processing time versus convolution window size Δk_x is shown for the "open shielding" configuration scans.

Table 1:

Standard Deviation of EMI in the ROI outside object (see red box in Fig. 7) averaged across partitions for all subjects in the open and flexible shielding configurations for the uncorrected and corrected images.

Subject	Flexible Shielding ($\sigma \times 10^6$)		Open Shielding ($\sigma \times 10^6$)	
	Uncorrected	Corrected	Uncorrected	Corrected
Subject 1	17.5	5.36	78.9	20.2
Subject 2	9.92	6.09	41.5	13.9
Subject 3	30.7	6.49	57.1	16.2